

Quantum-metric-induced nonlinear transport in a topological antiferromagnet

<https://doi.org/10.1038/s41586-023-06363-3>

Received: 16 January 2023

Accepted: 22 June 2023

Published online: 29 June 2023

 Check for updates

Naizhou Wang¹, Daniel Kaplan², Zhaowei Zhang¹, Tobias Holder², Ning Cao³, Aifeng Wang³, Xiaoyuan Zhou³, Feifei Zhou¹, Zhengzhi Jiang¹, Chusheng Zhang¹, Shihao Ru¹, Hongbing Cai^{1,4}, Kenji Watanabe⁵, Takashi Taniguchi⁶, Binghai Yan² & Weibo Gao^{1,4,7}

The Berry curvature and quantum metric are the imaginary part and real part, respectively, of the quantum geometric tensor, which characterizes the topology of quantum states¹. The Berry curvature is known to generate a number of important transport phenomena, such as the quantum Hall effect and the anomalous Hall effect^{2,3}; however, the consequences of the quantum metric have rarely been probed by transport measurements. Here we report the observation of quantum-metric-induced nonlinear transport, including both a nonlinear anomalous Hall effect and a diode-like non-reciprocal longitudinal response, in thin films of a topological antiferromagnet, MnBi₂Te₄. Our observations reveal that the transverse and longitudinal nonlinear conductivities reverse signs when reversing the antiferromagnetic order, diminish above the Néel temperature and are insensitive to disorder scattering, thus verifying their origin in the band-structure topology. They also flip signs between electron- and hole-doped regions, in agreement with theoretical calculations. Our work provides a means to probe the quantum metric through nonlinear transport and to design magnetic nonlinear devices.

Nonlinear transport provides a powerful tool for probing topological physics in solids^{4–21}. A prime example of this is the nonlinear anomalous Hall effect (NLAHE), which reveals the Berry curvature dipole on the Fermi surface and has recently been observed in non-magnetic topological semimetals^{6,9,10,12,14,15} (as shown in Fig. 1a). This provides a powerful means of investigating quantum geometry in flat space. Another NLAHE caused by the quantum metric, the counterpart of the Berry curvature in the quantum geometry, has also been predicted for magnetic topological materials, but is yet to be realized in experiments^{1,22–30}. The quantum metric measures the amplitude distance between two neighbouring Bloch states and determines the electronic properties of a crystal. A recent theory^{26,30} finds that the quantum metric actually gives rise to both the NLAHE and the non-reciprocal longitudinal response, the latter of which is characterized by a diode-like longitudinal resistance, in inversion-breaking magnetic materials⁷ (as shown in Fig. 1b). The asymmetric quantum metric (quantum metric dipole) induces an anomalous motion of the wave packet and generates nonlinear responses in both the longitudinal and transverse directions. As the quantum metric is antisymmetric under momentum inversion ($k \rightarrow -k$), both time-reversal symmetry (T) and inversion symmetry (P) must be broken to generate a net quantum metric dipole. In addition, the combined PT symmetry can exclude the contribution from the Berry curvature dipole⁴. As a result, a system that breaks both P and T but preserves PT is expected to be an ideal platform for studying the quantum metric effect (see Supplementary Section 1 for detailed symmetry analysis).

After careful consideration, we chose MnBi₂Te₄ as the candidate platform to investigate the quantum metric. Compared with the magnetic doped topological insulator, the intrinsic magnetic topological insulator, MnBi₂Te₄, has gained a lot of interest recently owing to its unique properties^{17,31–41}. As shown in Fig. 1c,e, the crystal structure of MnBi₂Te₄ consists of alternating layers of Te–Bi–Te–Mn–Te–Bi–Te, known as septuple layers (SLs)^{33,34}. MnBi₂Te₄ has an A-type antiferromagnetic (AFM) ground state, in which the Mn spins in each SL are aligned ferromagnetically with an out-of-plane easy axis but are coupled antiparallel to adjacent SLs. For even-layer MnBi₂Te₄, both P and T symmetry are broken but the combined PT symmetry is preserved below the Néel temperature³⁷. Figure 1d shows the spatial reflectance magnetic circular dichroism (RMCD) mapping of 3SL-MnBi₂Te₄ and 4SL-MnBi₂Te₄, measured at zero magnetic field, indicating fully compensated AFM states in even-layer MnBi₂Te₄ (ref. 40). In addition, MnBi₂Te₄ possesses three-fold rotational symmetry (from the optical second-harmonic generation (SHG) shown in Fig. 1f)⁴¹, which suppresses the Berry curvature dipole even in the absence of PT symmetry, making the contribution from the quantum metric much easier to observe³⁰.

Electron nonlinearity from spin order

To investigate the electron nonlinearity, we fabricated several high-quality, dual-gated even-layer MnBi₂Te₄ devices. Here we focus on a 4SL-MnBi₂Te₄ device, the schematic structure of which is shown in Fig. 2a. The dual-gate structure allows us to independently control

¹Division of Physics and Applied Physics, School of Physical and Mathematical Sciences, Nanyang Technological University, Singapore, Singapore. ²Department of Condensed Matter Physics, Weizmann Institute of Science, Rehovot, Israel. ³Low Temperature Physics Laboratory, College of Physics and Center of Quantum Materials and Devices, Chongqing University, Chongqing, China. ⁴The Photonics Institute and Centre for Disruptive Photonic Technologies, Nanyang Technological University, Singapore, Singapore. ⁵Research Center for Functional Materials, National Institute for Materials Science, Tsukuba, Japan. ⁶International Center for Materials Nanoarchitectonics, National Institute for Materials Science, Tsukuba, Japan. ⁷Centre for Quantum Technologies, National University of Singapore, Singapore, Singapore. [✉]e-mail: binghai.yan@weizmann.ac.il; wbgao@ntu.edu.sg

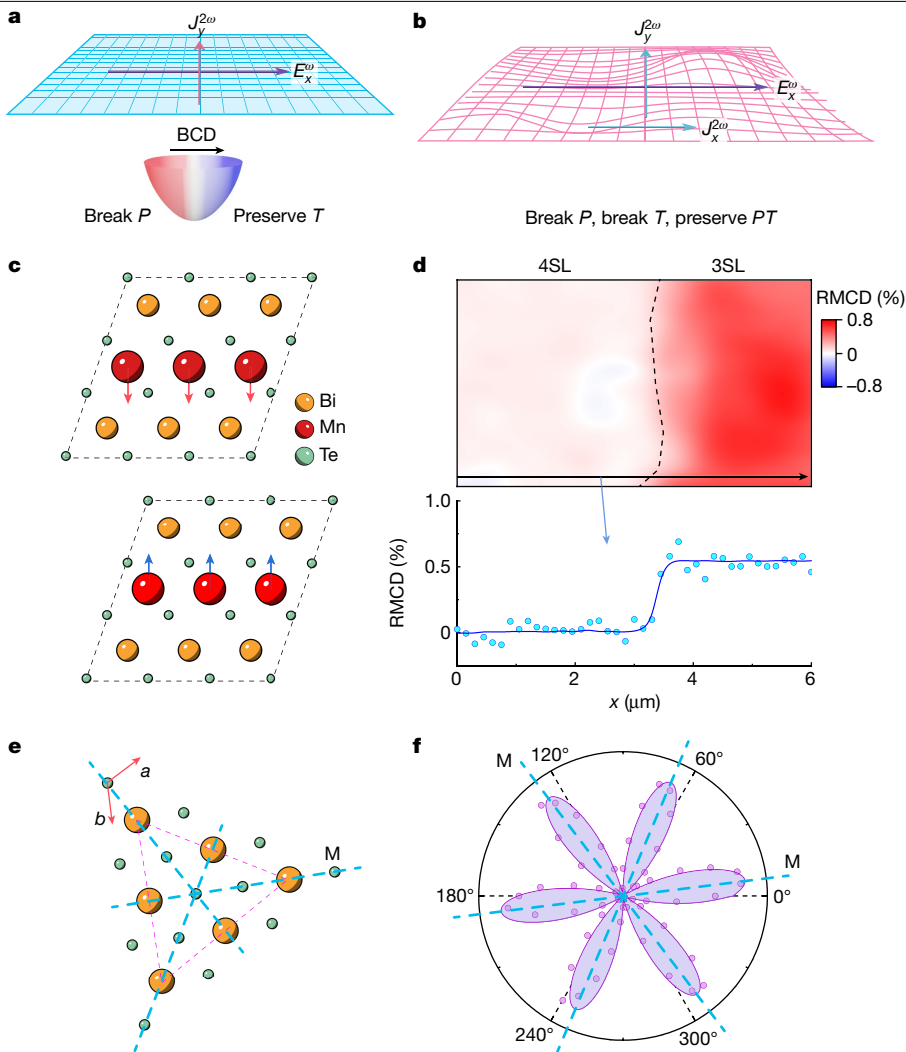


Fig. 1 | Quantum-metric-induced nonlinearity in a PT -symmetric AFM.

a, The nonlinear Hall effect originating from the Berry curvature dipole (BCD), which has been observed in systems with broken inversion symmetry. **b**, The nonlinear longitudinal and transverse response observed in a PT -symmetric system owing to the quantum metric dipole. **c**, The crystal structure of even-layer MnBi₂Te₄ from the side view. The arrows represent the spin-momentum

direction of the manganese atoms. **d**, The spatial RMCD mapping of MnBi₂Te₄ measured at zero magnetic field. The dashed line marks the boundary between 4SL-MnBi₂Te₄ and 3SL-MnBi₂Te₄. **e**, The crystal structure of MnBi₂Te₄ from the top view. The dashed line marked with M represents the mirror line. **f**, The angle-dependent optical SHG of the 4SL-MnBi₂Te₄ sample. The 0° corresponds to the applied current direction in the device.

the carrier density and vertical displacement field. As per theoretical predictions, the quantum metric gives rise to both the NL-AHE and the non-reciprocal longitudinal response³⁰. The former is directly measurable via an alternating current (a.c.) method, whereas the latter exhibits diode-like non-reciprocal resistance behaviour, expressed as $V_x = R_0(I + \gamma I^2)$ where I represents the applied current, R_0 is the linear resistance and γ denotes the coefficient characterizing the non-reciprocity⁷. Considering that the non-reciprocal longitudinal response stems from the quadratic term of the current, we adopted the a.c. method to measure the second-harmonic voltage $V_x^{2\omega}$ to reflect the non-reciprocal behaviour in the longitudinal direction, which offers a better signal-to-noise ratio (see Supplementary Section 4). To measure the linear and nonlinear responses of the device, we employed a standard lock-in technique. As depicted in Fig. 2a, an a.c. current with frequency of ω (I^ω) was injected, and the linear voltage V^ω and second-harmonic voltage $V^{2\omega}$ are simultaneously probed. In our experiment, the x axis is defined as the current direction and the y axis as the transverse direction to the current. All the measurements are conducted at $T = 1.8$ K in the absence of a magnetic field unless otherwise specified. Figure 2b shows the linear longitudinal (V_x^ω) and transverse

(V_y^ω) voltages, indicating good ohmic contact and a negligible misalignment in the Hall bar geometry from the vanishing of V_x^ω .

Next, we focus on the nonlinear responses of 4SL-MnBi₂Te₄ in opposite AFM states. Utilizing a method akin to those reported previously for controlling AFM states in chromium triiodide (CrI₃) or even-layer MnBi₂Te₄, we prepared the AFM-I and AFM-II states^{37,42} with opposite Néel orders. As shown in Fig. 2c,d, the AFM-I state is prepared by sweeping the magnetic field from -7 T to 0 T, whereas the AFM-II state is achieved by sweeping the magnetic field from $+7$ T to 0 T. For the linear responses, both AFM states exhibited identical longitudinal (V_x^ω) voltages, and the transverse (V_y^ω) voltages remained at zero (Extended Data Fig. 1). This observation aligns with the fully compensated AFM orders in 4SL-MnBi₂Te₄ (Extended Data Fig. 2). However, the nonlinear responses differ significantly from their linear counterparts. Focusing first on the AFM-I state, Fig. 2c shows that while the linear transverse (V_y^ω) voltage remains at zero, there is a significant negative nonlinear transverse voltage (notated as $V_y^{2\omega}$) that scales quadratically with the injected current I^ω . More importantly, we also detected a prominent negative nonlinear longitudinal voltage (denoted as $V_x^{2\omega}$), with the same order of magnitude as $V_y^{2\omega}$. This observation aligns with the prediction that the quantum

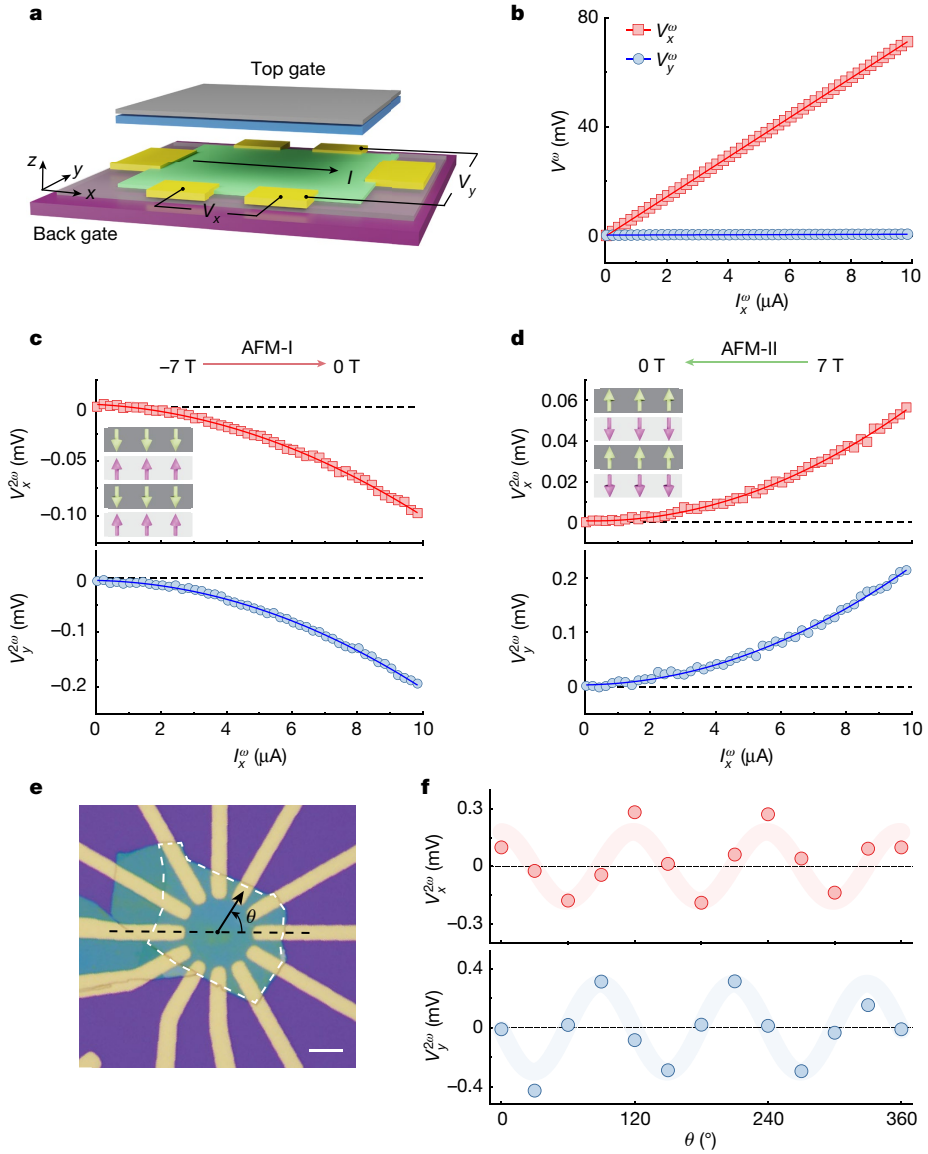


Fig. 2 | Observation of nonlinear transport in AFM MnBi₂Te₄. **a**, Schematic view of the dual-gated 4SL-MnBi₂Te₄ device. The linear and nonlinear signals are measured simultaneously with the denoted direction. **b**, The linear longitudinal V_x^ω and transverse V_y^ω voltage as a function of current I_x^ω . The solid line is the linear fitting of the data. **c,d**, The nonlinear longitudinal $V_x^{2\omega}$ (top) and transverse $V_y^{2\omega}$ (bottom) voltage as a function of current V_x^ω for the AFM-I (c) and AFM-II (d) states. At a fixed electric field, the different AFM states are prepared by: AFM-I,

sweeping the magnetic field from -7 T to 0 T; AFM-II, sweeping the magnetic field from $+7$ T to 0 T. The solid lines are quadratic fits to the data. **e**, Optical image of another 4SL-MnBi₂Te₄ device with radially distributed electrodes. The dashed line indicates the in-plane crystalline axis, determined by SHG measurement. Scale bar, 5 μ m. **f**, The nonlinear transverse $V_y^{2\omega}$ and longitudinal $V_x^{2\omega}$ response as a function of current injection angle θ .

metric dipole can induce both the nonlinear Hall and the non-reciprocal longitudinal responses, distinctly different from the response observed in the nonlinear Hall effect caused by the Berry curvature dipole, where only a Hall response is allowed and the longitudinal response is absent^{9,10}. The non-reciprocal longitudinal response in MnBi₂Te₄ can also be observed through d.c. measurements (Supplementary Section 4). Subsequently, we prepared the AFM-II state. As shown in Fig. 2d, in sharp contrast, although the amplitudes of $V_y^{2\omega}$ and $V_x^{2\omega}$ remain nearly the same with the AFM-I state, the sign of both flips to positive. The sign reversal of the nonlinear response suggests that the nonlinear response observed in MnBi₂Te₄ is associated with the AFM order. We carefully examined and ruled out potential alternative origins, such as a thermal effect or an accidental diode junction that could lead to a nonlinear effect. We also exclude the possibility that the nonlinear response observed in even-layer MnBi₂Te₄ is originated from the residual magnetization (Supplementary Section 2). To further confirm that the nonlinear signal is

an intrinsic response originating from the *PT*-symmetric AFM order, we investigate whether the nonlinear response complies with the rotational symmetry of AFM even-layer MnBi₂Te₄, where $\sigma_{yxz} = -\sigma_{yyz}$ and $\sigma_{xyy} = -\sigma_{xxx}$. When y aligns with the in-plane crystal axis, it should follow that $\sigma_{xyy} = -\sigma_{xxx} = 0$. The coexistence of $\sigma_{yxz}^{2\omega}$ and $\sigma_{xxx}^{2\omega}$ in this 4SL-MnBi₂Te₄ device suggests some misalignment between x/y and the crystal axes, consistent with our optical SHG measurement in Fig. 1f. To substantiate this further, we fabricated another 4SL-MnBi₂Te₄ device with radially distributed electrodes aligned to the crystalline axis (dashed line in Fig. 2e). Figure 2f shows the nonlinear transverse and longitudinal response upon rotation of the current injection direction. Both transverse $V_y^{2\omega}$ and longitudinal $V_x^{2\omega}$ exhibit three-fold symmetry. These observed features align consistently with the symmetry of the AFM even-layer MnBi₂Te₄.

We further investigated the temperature dependence of the nonlinear response in MnBi₂Te₄. Figure 3a,b shows the temperature-dependent

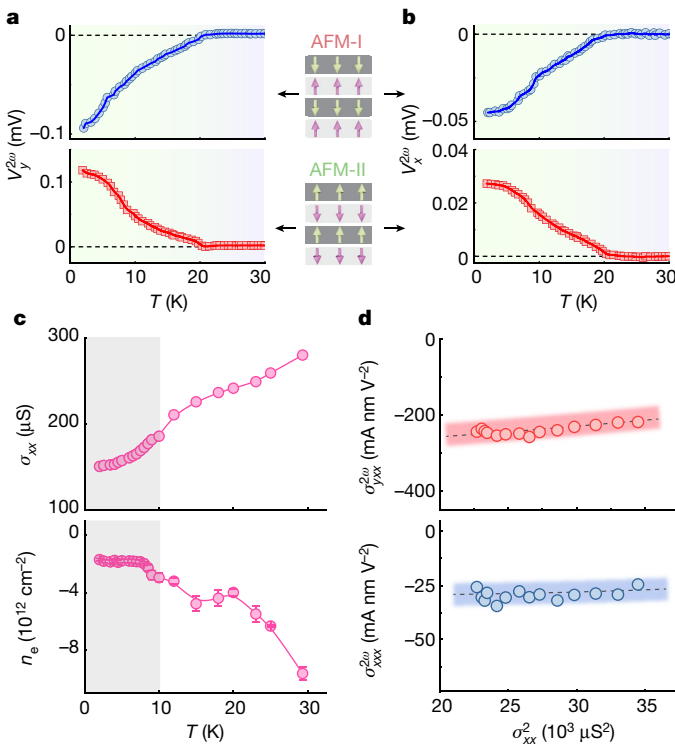


Fig. 3 | Spin-order-related electron nonlinearity from the band-normalized quantum metric dipole. **a**, Nonlinear transverse voltage $V_y^{2\omega}$ of 4SL-MnBi₂Te₄ as a function of temperature for opposite AFM-I (top) and AFM-II (bottom) states. The amplitudes of $V_y^{2\omega}$ are similar for the two AFM states but their sign is reversed. $V_y^{2\omega}$ vanishes when the temperature is above the Néel temperature of MnBi₂Te₄. **b**, The nonlinear longitudinal voltage $V_x^{2\omega}$ as a function of temperature for opposite AFM-I (top) and AFM-II (bottom) states, showing a similar trend to $V_y^{2\omega}$. **c**, The conductivity and fitted carrier density of 4SL-MnBi₂Te₄ at different temperatures. **d**, The scaling relationship between the nonlinear conductivity $\sigma_{yxx}^{2\omega}$ ($\sigma_{xxx}^{2\omega}$) and the square of the linear longitudinal conductivity σ_{xx}^{ω} . The scaling is carried out at the temperature range of 2–10 K (marked with shadow area in c), in which the carrier density nearly remains constant. The nonlinear transverse and longitudinal conductivities are extracted by $\sigma_{yxx}^{2\omega} = \frac{V_y^{2\omega}}{(I_x^{\omega})^2 R_{xx}^3 W^3}$ and $\sigma_{xxx}^{2\omega} = \frac{V_x^{2\omega}}{(I_x^{\omega})^2 R_{xx}^3}$, respectively. The dashed line is a fit of the data with the scaling relation $\sigma^{2\omega} = \eta_2 (\sigma_{xx}^{\omega})^2 + \eta_0$. From the fitting, we conclude that the predominant contribution is from the η_0 term, namely, from the intrinsic nonlinear conductivity owing to the band-normalized quantum metric dipole.

nonlinear voltages $V_y^{2\omega}$ and $V_x^{2\omega}$, which are prepared at AFM-I and AFM-II states, respectively. As the temperature increases, we found that the nonlinear voltage gradually decreases and vanishes above the Néel temperature of MnBi₂Te₄, indicating that the nonlinear response is absent in the non-magnetic states. In addition, the nonlinear response in even-layer MnBi₂Te₄ is presented only at the AFM states and vanishes when all spins are aligned in one direction (see details in Supplementary Section 3). In summary, we can conclude that the nonlinear response observed is associated with the nonlinearity of electron motion originating from the AFM order in 4SL-MnBi₂Te₄.

Quantum-metric-induced nonlinear transport

We now systematically investigate the microscopic origin of the nonlinear response observed in 4SL-MnBi₂Te₄. To quantify the strength of the nonlinear response, we use the nonlinear conductivity, as it is independent of the sample size. In our experiment, we can extract the longitudinal and transverse nonlinear conductivity from our data as $\sigma_{xxx}^{2\omega} = \frac{J_x^{2\omega}}{(E_{xx}^{\omega})^2} = \frac{V_x^{2\omega} L}{(I_x^{\omega})^2 R_{xx}^3}$ and $\sigma_{yxx}^{2\omega} = \frac{J_x^{2\omega}}{(E_{xx}^{\omega})^2} = \frac{V_y^{2\omega} L}{(I_x^{\omega})^2 R_{xx}^3 W^2}$, respectively, where L

and W are the longitudinal and transverse length of the Hall bar device. In theory, the nonlinear conductivity due to an applied electric field E_x in a metal includes three contributions³⁰

$$J_c = \sigma_{cxx} E_x^2 = (\sigma_{cxx}^2 + \sigma_{cxx}^1 + \sigma_{cxx}^0) E_x^2 \quad (1)$$

where σ_{cxx}^i has the i th order of τ dependence ($c = x$ or $c = y$). Here $\sigma_{cxx}^2 = -\frac{e^3 \tau^2}{\hbar^3} \int d^2 k f_n \partial_{k_c} \partial_{k_x} \epsilon_n(\mathbf{k})$ is the nonlinear Drude weight, and $\epsilon_n(\mathbf{k})$ is the energy of Bloch state n at momentum \mathbf{k} , and f_n is the Fermi Dirac distribution for band n . $\sigma_{cxx}^1 = -\frac{e^3 \tau}{\hbar^2} \int d^2 k f_n (2 \partial_{k_x} G_n^{xc})$, is the Berry curvature dipole contribution⁴, where e is the elementary charge, τ is the scattering time and \hbar is the reduced Planck constant. The conductivity due to the normalized dipole of the quantum metric is³⁰

$$\sigma_{baa}^0 = -\frac{e^3}{\hbar^2} \int d^2 k f_n (2 \partial_{k_b} G_n^{aa} - \partial_{k_a} G_n^{ab}) \quad (2)$$

where $a/b = x/y$, $G_n^{ab} = \sum_{m \neq n} \frac{A_{nm}^a A_{nm}^b + A_{nm}^b A_{nm}^a}{(\epsilon_n - \epsilon_m)}$ is the band-energy normalized quantum metric (A_{mn}^a is the interband Berry connection, and n and m are band indices) and $\partial_{k_a} G_n^{ab}$ represents the normalized quantum metric dipole. In the specific case of 4SL-MnBi₂Te₄, the *PT* symmetry excludes any contribution from the Berry curvature dipole⁴. In addition, the Berry curvature dipole contribution, which is even under time reversal, contradicts the sign reversal of the nonlinear signal between the AFM-I and AFM-II phases. It is also worth noting that the skew scattering mechanism can also contribute to the nonlinear response^{21,43}, which is significantly suppressed by *PT* symmetry⁴⁴. Although the anomalous skew scattering is not excluded by *PT* symmetry⁴⁵ we can exclude its contribution based on the scaling analysis discussed subsequently. Therefore, the intrinsic contributions to the nonlinear conductivity in MnBi₂Te₄ are determined by the nonlinear Drude weight and the normalized quantum metric dipole.

To verify the dominant contribution from the quantum metric, we investigate the scaling relationship between nonlinear conductivities ($\sigma_{yxx}^{2\omega}$ and $\sigma_{xxx}^{2\omega}$) and the linear conductivity σ_{xx}^{ω} (that is, scattering time τ) as a function of temperature. Figure 3c shows the temperature dependence of longitudinal conductivity σ_{xx}^{ω} and charge carrier density n_e . The charge carrier density n_e remains almost unchanged at the temperature of 1.6 K to 10 K, suggesting that the τ is the main component to determine the conductivity σ_{xx}^{ω} in this range. By adopting this range, we plot $\sigma_{yxx}^{2\omega}$ and $\sigma_{xxx}^{2\omega}$ as a function of conductivity $(\sigma_{xx}^{\omega})^2$ and fit with the formula,

$$\sigma^{2\omega} = \eta_2 (\sigma_{xx}^{\omega})^2 + \eta_0 \quad (3)$$

which is shown in Fig. 3d. We find that the predominant contribution to both $\sigma_{xxx}^{2\omega}$ and $\sigma_{yxx}^{2\omega}$ is the intrinsic nonlinear conductivity from the normalized quantum metric dipole (η_0 , τ -independent term). The nonlinear Drude contribution (η_2 , τ^2 -dependent term) is nearly negligible compared with the intrinsic one, which is reasonable considering the small conductivity and low mobility in MnBi₂Te₄. The dominant τ -independent nonlinear conductivity further excludes a contribution from the impurity scattering, because its lowest-order contribution to the nonlinear conductivity begins at τ^1 (see detailed discussion in Supplementary Section 7.2)^{21,43}. In conclusion, we attribute the nonlinear response observed in 4SL-MnBi₂Te₄ to the nonlinear Drude weight and the normalized quantum metric dipole, with the latter being the dominant contributor.

Fermi-energy-dependent nonlinear response

We next study how the nonlinear conductivity in 4SL-MnBi₂Te₄, originating from normalized quantum metric dipole, is influenced by the vertical displacement electric field (denoted as D) and the electron charge carrier density (denoted as n_e). Figure 4a shows the resistance of 4SL-MnBi₂Te₄ as a function of top (V_{TG}) and bottom (V_{BG}) gate

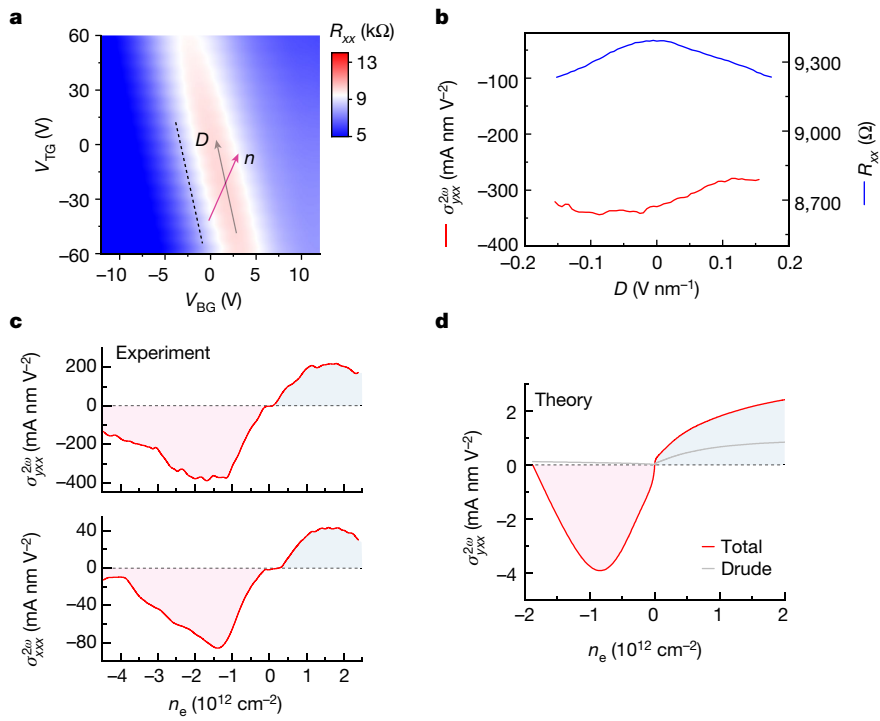


Fig. 4 | The electric-field and carrier-density-dependence of the nonlinear response. **a**, The resistance map of the 4SL-MnBi₂Te₄ device. The vertical displacement field D and charge carrier density n_e can be independently controlled, as denoted in the figure. **b**, The nonlinear transverse conductivity $\sigma_{yxx}^{2\omega}$ and longitudinal resistance R_{xx} as a function of vertical displacement electric field. The carrier density is fixed at $n_e \approx -3 \times 10^{-12} \text{ cm}^{-2}$ as D varies along

the dashed line in **a**. **c**, The measured nonlinear transverse conductivity $\sigma_{yxx}^{2\omega}$ (top) and longitudinal conductivity $\sigma_{xxx}^{2\omega}$ (bottom) as a function of charge carrier density n_e . **d**, The calculated total nonlinear transverse conductivity $\sigma_{yxx}^{2\omega}$ (red line) as a function of carrier density. The grey line denotes the Drude contribution.

voltages, with the direction of D and n_e labelled in the figure. We first examine the effect of D on the nonlinear response. Although PT symmetry is instrumental in isolating the quantum-metric-dipole contribution, the induced nonlinear response remains even when PT is broken by D . Furthermore, we note that the Berry-curvature-dipole-induced NLAHE still vanishes because of three-fold rotational symmetry. To demonstrate this, we investigate the dependence of $\sigma_{yxx}^{2\omega}$ on the electric field D with fixed carrier density at $n_e \approx -3 \times 10^{-12} \text{ cm}^{-2}$. As shown in Fig. 4b, $\sigma_{yxx}^{2\omega}$ changes only slightly when tuning the electric field away from $D = 0$. Next, we investigate the effect of charge carrier density n_e on the nonlinear response. Figure 4c shows the nonlinear conductivity $\sigma_{yxx}^{2\omega}$ and $\sigma_{xxx}^{2\omega}$ as a function of carrier density n_e , respectively. When the Fermi level is tuned into the charge-neutral gap, both $\sigma_{yxx}^{2\omega}$ and $\sigma_{xxx}^{2\omega}$ vanish. This is in line with the fact that the quantum metric dipole is a Fermi surface property³⁰. Furthermore, both $\sigma_{yxx}^{2\omega}$ and $\sigma_{xxx}^{2\omega}$ show a sign reversal when tuning the carrier density between hole and electron regimes. Lastly, given the evident non-reciprocal longitudinal response, we can evaluate the non-reciprocity coefficient γ in MnBi₂Te₄. We find that the coefficient γ can reach $\gamma \approx 7 \times 10^{-11} \text{ m}^2 \text{ A}^{-1}$, which is two or three orders larger than traditional heavy metal/ferromagnetic metal heterostructures (see details in Supplementary Section 4.3)^{46,47}.

To explain our experimental data, we evaluate $\sigma_{yxx}^{2\omega}$ quantitatively by constructing a slab model for 4SL-MnBi₂Te₄ with density-functional theory calculations. Figure 4d shows the total conductivity as a function of carrier density, in which we assume $\sigma_{yxx}^{2\omega}$ for an ideally aligned device (y aligned with the in-plane crystalline axis). Importantly, around the charge-neutrality gap ($\mu = 0$), we observe a sign change which reproduces the experimental findings (see Supplementary Section 7.1 for the band-resolved contributions to the quantum metric). The deviation of theoretical $\sigma_{yxx}^{2\omega}$ compared with experimental values may be attributed to the known discrepancy in surface band structure between

calculations and experiments on MnBi₂Te₄. In addition, in our calculation, we find that the Drude contribution is small within a large energy range around the Fermi level, indicating that the nonlinear conductivity is primarily driven by the quantum metric dipole. We conducted similar measurements on another 6SL-MnBi₂Te₄ device, as detailed in Supplementary Section 6.

As a probe, the quantum-metric-dipole-driven electron nonlinearity in MnBi₂Te₄ has several advantages and holds great promise for future applications. First, compared with nonlinearity originating from the Berry curvature dipole or skew scattering, the quantum-metric-dipole-driven electron nonlinearity is independent of the scattering time, suggesting its robustness against disorder scattering. Second, the quantum-metric-dipole-driven electron nonlinearity is distinct for opposite AFM spin orders and even robust against small perturbations of external magnetic fields (see details in Supplementary Section 3), making it a promising candidate for use as a nonlinear magnetic memory device. Finally, the quantum-metric-dipole-driven nonlinear response is more prominent than the ‘traditional’ nonlinear response from the Berry curvature dipole. We compared the nonlinear response observed in MnBi₂Te₄ with other two-dimensional material systems, as shown in Extended Data Table 1. We find that our MnBi₂Te₄ devices have a much larger nonlinear conductivity than WTe₂ and strained WSe₂, only smaller than twisted WSe₂ and graphene Moiré superlattices, making MnBi₂Te₄ a promising candidate for highly efficient rectifying devices^{9,10,13,16,19}.

Online content

Any methods, additional references, Nature Portfolio reporting summaries, source data, extended data, supplementary information, acknowledgements, peer review information; details of author

contributions and competing interests; and statements of data and code availability are available at <https://doi.org/10.1038/s41586-023-06363-3>.

1. Provost, J. P. & Vallee, G. Riemannian structure on manifolds of quantum states. *Commun. Math. Phys.* **76**, 289–301 (1980).
2. Thouless, D. J., Kohmoto, M., Nightingale, M. P. & den Nijs, M. Quantized Hall conductance in a two-dimensional periodic potential. *Phys. Rev. Lett.* **49**, 405–408 (1982).
3. Nagaosa, N., Sinova, J., Onoda, S., MacDonald, A. H. & Ong, N. P. Anomalous Hall effect. *Rev. Mod. Phys.* **82**, 1539–1592 (2010).
4. Sodemann, I. & Fu, L. Quantum nonlinear Hall effect induced by Berry curvature dipole in time-reversal invariant materials. *Phys. Rev. Lett.* **115**, 216806 (2015).
5. Ideue, T. et al. Bulk rectification effect in a polar semiconductor. *Nat. Phys.* **13**, 578–583 (2017).
6. Du, Z. Z., Wang, C. M., Lu, H. Z. & Xie, X. C. Band signatures for strong nonlinear Hall effect in bilayer WTe₂. *Phys. Rev. Lett.* **121**, 266601 (2018).
7. Tokura, Y. & Nagaosa, N. Nonreciprocal responses from non-centrosymmetric quantum materials. *Nat. Commun.* **9**, 3740 (2018).
8. Zhang, Y., Sun, Y. & Yan, B. Berry curvature dipole in Weyl semimetal materials: an ab initio study. *Phys. Rev. B* **97**, 041101 (2018).
9. Kang, K., Li, T., Sohn, E., Shan, J. & Mak, K. F. Nonlinear anomalous Hall effect in few-layer WTe₂. *Nat. Mater.* **18**, 324–328 (2019).
10. Ma, Q. et al. Observation of the nonlinear Hall effect under time-reversal-symmetric conditions. *Nature* **565**, 337–342 (2019).
11. Lai, S. et al. Third-order nonlinear Hall effect induced by the Berry-connection polarizability tensor. *Nat. Nanotechnol.* **16**, 869–873 (2021).
12. Kumar, D. et al. Room-temperature nonlinear Hall effect and wireless radiofrequency rectification in Weyl semimetal Ta_{1-x}Te_x. *Nat. Nanotechnol.* **16**, 421–425 (2021).
13. Qin, M.-S. et al. Strain tunable Berry curvature dipole, orbital magnetization and nonlinear Hall effect in WSe₂ monolayer. *Chin. Phys. Lett.* **38**, 017301 (2021).
14. Tiwari, A. et al. Giant c-axis nonlinear anomalous Hall effect in Td-MoTe₂ and WTe₂. *Nat. Commun.* **12**, 2049 (2021).
15. Du, Z. Z., Lu, H.-Z. & Xie, X. C. Nonlinear Hall effects. *Nat. Rev. Phys.* **3**, 744–752 (2021).
16. He, P. et al. Graphene moiré superlattices with giant quantum nonlinearity of chiral Bloch electrons. *Nat. Nanotechnol.* **17**, 378–383 (2022).
17. Zhang, Z. et al. Controlled large non-reciprocal charge transport in an intrinsic magnetic topological insulator MnBi₂Te₄. *Nat. Commun.* **13**, 6191 (2022).
18. Sinha, S. et al. Berry curvature dipole senses topological transition in a moiré superlattice. *Nat. Phys.* **18**, 765–770 (2022).
19. Huang, M. et al. Giant nonlinear Hall effect in twisted bilayer WSe₂. *Natl Sci. Rev.* **10**, nwac232 (2022).
20. Godinho, J. et al. Electrically induced and detected Néel vector reversal in a collinear antiferromagnet. *Nat. Commun.* **9**, 4686 (2018).
21. Isobe, H., Xu, S.-Y. & Fu, L. High-frequency rectification via chiral Bloch electrons. *Sci. Adv.* **6**, eaay2497 (2020).
22. Gao, Y., Yang, S. A. & Niu, Q. Field induced positional shift of Bloch electrons and its dynamical implications. *Phys. Rev. Lett.* **112**, 166601 (2014).
23. Wang, C., Gao, Y. & Xiao, D. Intrinsic nonlinear Hall effect in antiferromagnetic tetragonal CuMnAs. *Phys. Rev. Lett.* **127**, 277201 (2021).
24. Liu, H. et al. Intrinsic second-order anomalous Hall effect and its application in compensated antiferromagnets. *Phys. Rev. Lett.* **127**, 277202 (2021).
25. Watanabe, H. & Yanase, Y. Chiral photocurrent in parity-violating magnet and enhanced response in topological antiferromagnet. *Phys. Rev. X* **11**, 011001 (2021).
26. Holder, T., Kaplan, D., Ilan, R. & Yan, B. Mixed axial-gravitational anomaly from emergent curved spacetime in nonlinear charge transport. Preprint at <https://arxiv.org/abs/2111.07780> (2021).
27. Lahiri, S., Das, K., Culcer, D. & Agarwal, A. Intrinsic nonlinear conductivity induced by the quantum metric dipole. Preprint at <https://arxiv.org/abs/2207.02178> (2022).
28. Smith, T. B., Pullasser, L. & Srivastava, A. Momentum-space gravity from the quantum geometry and entropy of Bloch electrons. *Phys. Rev. Res.* **4**, 013217 (2022).
29. Arora, A., Rudner, M. S. & Song, J. C. W. Quantum plasmonic nonreciprocity in parity-violating magnets. *Nano Lett.* **22**, 9351–9357 (2022).
30. Kaplan, D., Holder, T. & Yan, B. Unification of nonlinear anomalous Hall effect and nonreciprocal magnetoresistance in metals by the quantum geometry. Preprint at <https://arxiv.org/abs/2211.17213> (2022).
31. Chang, C.-Z. et al. Experimental observation of the quantum anomalous Hall effect in a magnetic topological insulator. *Science* **340**, 167–170 (2013).
32. Otkrov, M. M. et al. Prediction and observation of an antiferromagnetic topological insulator. *Nature* **576**, 416–422 (2019).
33. Li, J. et al. Intrinsic magnetic topological insulators in van der Waals layered MnBi₂Te₄-family materials. *Sci. Adv.* **5**, eaaw5685 (2019).
34. Zhang, D. et al. Topological axion states in the magnetic insulator MnBi₂Te₄ with the quantized magnetoelectric effect. *Phys. Rev. Lett.* **122**, 206401 (2019).
35. Deng, Y. et al. Quantum anomalous Hall effect in intrinsic magnetic topological insulator MnBi₂Te₄. *Science* **367**, 895–900 (2020).
36. Liu, C. et al. Robust axion insulator and Chern insulator phases in a two-dimensional antiferromagnetic topological insulator. *Nat. Mater.* **19**, 522–527 (2020).
37. Gao, A. et al. Layer Hall effect in a 2D topological axion antiferromagnet. *Nature* **595**, 521–525 (2021).
38. Deng, H. et al. High-temperature quantum anomalous Hall regime in a MnBi₂Te₄/Bi₂Te₃ superlattice. *Nat. Phys.* **17**, 36–42 (2021).
39. Cai, J. et al. Electric control of a canted-antiferromagnetic Chern insulator. *Nat. Commun.* **13**, 1668 (2022).
40. Yang, S. et al. Odd–even layer-number effect and layer-dependent magnetic phase diagrams in MnBi₂Te₄. *Phys. Rev. X* **11**, 011003 (2021).
41. Fonseca, J. et al. Anomalous second harmonic generation from atomically thin MnBi₂Te₄. *Nano Lett.* **22**, 10134–10139 (2022).
42. Jiang, S., Shan, J. & Mak, K. F. Electric-field switching of two-dimensional van der Waals magnets. *Nat. Mater.* **17**, 406–410 (2018).
43. Du, Z. Z., Wang, C. M., Li, S., Lu, H.-Z. & Xie, X. C. Disorder-induced nonlinear Hall effect with time-reversal symmetry. *Nat. Commun.* **10**, 3047 (2019).
44. Watanabe, H. & Yanase, Y. Nonlinear electric transport in odd-parity magnetic multipole systems: application to Mn-based compounds. *Phys. Rev. Res.* **2**, 043081 (2020).
45. Ma, D., Arora, A., Vignale, G. & Song, J. C. Anomalous skew-scattering nonlinear Hall effect in PT-symmetric antiferromagnets. Preprint at <https://arxiv.org/abs/2210.14932> (2022).
46. Avci, C. O. et al. Unidirectional spin Hall magnetoresistance in ferromagnet/normal metal bilayers. *Nat. Phys.* **11**, 570–575 (2015).
47. Avci, C. O., Mendil, J., Beach, G. S. D. & Gambardella, P. Origins of the unidirectional spin Hall magnetoresistance in metallic bilayers. *Phys. Rev. Lett.* **121**, 087207 (2018).

Publisher's note Springer Nature remains neutral with regard to jurisdictional claims in published maps and institutional affiliations.

Springer Nature or its licensor (e.g. a society or other partner) holds exclusive rights to this article under a publishing agreement with the author(s) or other rightsholder(s); author self-archiving of the accepted manuscript version of this article is solely governed by the terms of such publishing agreement and applicable law.

© The Author(s), under exclusive licence to Springer Nature Limited 2023

Methods

MnBi₂Te₄ single-crystal growth

Single crystals of MnBi₂Te₄ were grown using a self-flux method^{48,49}. The starting materials used in the single-crystal processes are manganese slices, bismuth lumps and tellurium chunks. MnTe and Bi₂Te₃ precursors were prepared by reacting the mixed stoichiometric starting materials at 1,100 °C and 900 °C for 24 h, respectively. Then MnTe and Bi₂Te₃ were mixed according to the ratio MnTe:Bi₂Te₃ = 15:85, loaded into an alumina crucible and sealed in a quartz tube. The quartz tube was heated to 650 °C in 10 h, dwelled for 12 h and slowly cooled to 595 °C at a rate of 1 °C per hour to grow the single crystals. Shiny, single crystals with a typical size of 3 × 2 × 0.5 mm³ can be obtained after centrifuging.

Device fabrication

The MnBi₂Te₄ thin flakes were obtained using the aluminium oxide (Al₂O₃)-assisted exfoliation method^{35,50}. First, a 70-nm-thick layer of Al₂O₃ was thermally evaporated onto bulk MnBi₂Te₄ crystals. Second, the Al₂O₃ thin film was lifted along with thin flakes of MnBi₂Te₄, which were cleaved from the bulk crystal using thermal release tape. Then, the stacked MnBi₂Te₄/Al₂O₃ was transferred onto a transparent poly-dimethylsiloxane film. The number of layers in the MnBi₂Te₄ thin flakes was determined using optical transmittance measurements. After confirming the layer number, the MnBi₂Te₄ thin-flake samples were transferred to a silicon wafer coated with 285 nm of silicon dioxide (SiO₂). To ensure high-quality samples, we used a stencil mask method to deposit metal contacts (chromium/gold) on the samples. A 20–40-nm-thick hexagonal boron nitride (hBN) flake was then transferred to the MnBi₂Te₄ devices as the top-gate dielectric layer, followed by the transfer of a graphite thin-flake gate on top of the hBN/MnBi₂Te₄ heterostructure. The entire device fabrication process was carried out in a nitrogen-filled glove box with oxygen and water levels below 1 ppm.

Nonlinear electrical transport measurements

The electrical transport measurements were performed in a cryogenic-free cryostat equipped with a superconducting magnet (Cryomagnetic). We used a standard lock-in technique (Zurich MFLI) with excitation frequencies ranging from 10 Hz to 200 Hz to measure both the first- and second-harmonic signals. The data presented in this paper were collected at a low frequency of 17.777 Hz. During the transport measurements, the phase of the first- and second-harmonic signals was confirmed to be approximately 0° and 90°, respectively (Supplementary Section 2.4). The gate voltages were applied using a Keithley 2636 SourceMeter. To independently control the charge carrier density n_e and displacement electric field D , we used a dual-gated device structure. The charge carrier density n can be obtained

$$\text{by } n = \left(\frac{\varepsilon_0 \epsilon^{\text{BN}} (V_{TG} - V_{TGO})}{d_{BN}} + \varepsilon_0 (V_{BG} - V_{BGO}) \right) / \left(\frac{d_{Al_2O_3}}{\varepsilon^{Al_2O_3}} + \frac{d_{SiO_2}}{\varepsilon^{SiO_2}} \right) / e. \text{ Here we regarded the Al}_2\text{O}_3 \text{ and SiO}_2 \text{ dielectric layer as two series connected capacitors.}$$

The electric displacement field D can be obtained

$$\text{by } D = \left(\frac{V_{BG} - V_{BGO}}{\left(\frac{d_{Al_2O_3}}{\varepsilon^{Al_2O_3}} + \frac{d_{SiO_2}}{\varepsilon^{SiO_2}} \right)} - \frac{\varepsilon^{\text{BN}} (V_{TG} - V_{TGO})}{d_{BN}} \right) / 2. \text{ Here, } \varepsilon_0 \text{ is the vacuum permittivity; } V_{TGO} \text{ and } V_{BGO} \text{ correspond to the top-gate and bottom-gate voltage of maximum resistance, respectively; } \varepsilon^{Al_2O_3}, \varepsilon^{SiO_2} \text{ and } \varepsilon^{\text{BN}} \text{ are the relative dielectric constant of Al}_2\text{O}_3, \text{SiO}_2 \text{ and hBN; } d_{Al_2O_3}, d_{SiO_2} \text{ and } d_{BN} \text{ are the thickness of Al}_2\text{O}_3, \text{SiO}_2 \text{ and hBN, respectively. We noticed a minor asymmetry in } \sigma_{yxx}^{2\omega} \text{ and } R_{xx} \text{ with respect to the displacement electric field } D, \text{ possibly attributed to charge trapping induced by substrate effects or disorder}^{51}. \text{ The asymmetry is more pronounced in } \sigma_{yxx}^{2\omega} \text{ as the quantum metric is related to energy differences between bands and more sensitive to } D.$$

Nonlinear response in the MnBi₂Te₄ device with radially distributed devices

For the MnBi₂Te₄ device with radially distributed electrodes, when the current aligns with the in-plane crystal axis ($\theta = 0^\circ$), the transverse $V_y^{2\omega}$ is zero. In contrast, when the current is perpendicular to the crystalline axis ($\theta = 90^\circ$), the longitudinal $V_x^{2\omega}$ is zero. In addition, the nonlinear response should obey the symmetry of even-layer MnBi₂Te₄, with $\sigma_{yxx} = -\sigma_{yyy}$ and $\sigma_{xxy} = -\sigma_{xxx}$. To substantiate this, we use the formula for nonlinear conductivity: $\sigma_{xxx}^{2\omega} = \frac{J_x^{2\omega}}{(E_{xx}^{2\omega})^2} = \frac{V_x^{2\omega} L}{(E_{xx}^{2\omega})^2 R_{xx}^3}$ and $\sigma_{yxx}^{2\omega} = \frac{J_y^{2\omega}}{(E_{xx}^{2\omega})^2} = \frac{V_y^{2\omega} L^3}{(E_{xx}^{2\omega})^2 R_{xx}^3 W^2}$. Here, L refers to the length and W to the width of the device. The optical image (Fig. 2e) reveals that the length-to-width ratio, L/W , is approximately 0.85. Taking into consideration the geometric characteristics of the device, we conclude that the nonlinear conductivity conforms to $\sigma_{yxx} = -\sigma_{yyy}$ and $\sigma_{xxy} = -\sigma_{xxx}$.

Optical measurement

For the RMCD measurement, a linearly polarized 633-nm helium-neon laser was modulated by a photoelastic modulator at a frequency of 50 kHz. The laser beam was focused on the sample at normal incidence using an Olympus MPLN ×50 objective with a 0.75 numerical aperture. The laser spot size was approximately 2 μm, with a power of 1.8 μW. The reflected light was collected by a photodetector and analysed using a lock-in amplifier set to the same frequency as the photoelastic modulator. The RMCD measures the differential reflection between left- and right-circularly polarized light, the magnitude of which is proportional to the magnetic moments of the MnBi₂Te₄ sample.

The SHG measurement was performed at room temperature using femtosecond pulse lasers with a central wavelength of 800 nm. The laser beam was focused at normal incidence on the sample using a Nikon ELWD ×100 microscope objective. The SHG signals were collected using a spectrometer. To perform the polarization-resolved measurement, a motorized polarizer was used to control the polarization of the incident laser beam as it was rotated next to the objective.

Density-functional theory calculations

We used the Vienna Ab-initio Software Package with the Perdew-Burke-Ernzerhof functional in the generalized gradient approximation to obtain the electronic ground state⁵². We then projected the ground-state wavefunctions on Wannier functions using Wannier 90⁵³ and created a tight-binding model with 184 Wannier orbitals. For the Drude contribution, we adopted a lifetime of $\tau \approx 40$ fs estimated from our experimental conductivity and carrier density in Fig. 3c and theoretical effective mass ($m^* = 0.14 m_e$) for the 4SL film (m_e is the rest mass of an electron).

Data availability

Source data are provided with this paper.

48. Cao, N. et al. Angle dependent field-driven reorientation transitions in uniaxial antiferromagnet MnBi₂Te₄ single crystal. *Appl. Phys. Lett.* **120**, 163102 (2022).
49. Hu, C. et al. A van der Waals antiferromagnetic topological insulator with weak interlayer magnetic coupling. *Nat. Commun.* **11**, 97 (2020).
50. Deng, Y. et al. Gate-tunable room-temperature ferromagnetism in two-dimensional Fe₃GeTe₂. *Nature* **563**, 94–99 (2018).
51. Fei, Z. et al. Ferroelectric switching of a two-dimensional metal. *Nature* **560**, 336–339 (2018).
52. Kresse, G. & Furthmüller, J. Efficient iterative schemes for ab initio total-energy calculations using a plane-wave basis set. *Phys. Rev. B* **54**, 11169–11186 (1996).
53. Mostofi, A. A. et al. An updated version of Wannier 90: a tool for obtaining maximally-localised Wannier functions. *Comput. Phys. Commun.* **185**, 2309–2310 (2014).

Acknowledgements We thank S. A. Yang, H. Liu, S. Xu and J. Song for discussions. W.G. acknowledges the financial support from the Singapore National Research Foundation through its Competitive Research Program (CRP Award No. NRF-CRP22-2019-0004). B.Y. acknowledges

Article

the financial support by the European Research Council (ERC Consolidator Grant No. 815869, 'NonlinearTopo') and Israel Science Foundation (ISF No. 2932/21). A.W. acknowledges the financial support from the National Natural Science Foundation of China (grant no. 12004056), Chongqing Research Program of Basic Research and Frontier Technology, China (grant no. cstc2021jcyj-msxmX0661) and Fundamental Research Funds for the Central Universities, China (grant no. 2022CDJXY-002). X.Z. acknowledges the financial support from the National Key Research and Development Program of the Ministry of Science and Technology of China (2019YFA0704901) and the National Natural Science Foundation of China (grant nos. 52125103 and 52071041).

Author contributions W.G. and B.Y. conceived and supervised the project. N.W. fabricated the devices and performed the transport and RMCD measurements with help from Z.Z. and C.Z. D.K., T.H. and B.Y. performed the theoretical calculations. N.W. and F.Z. performed the NV measurement with help from Z.J., S.R. and H.C. N.W., W.G., D.K., T.H.

and B.Y. analysed the data. N.C., A.W. and X.Z. grew the MnBi_2Te_4 single crystals. K.W. and T.T. grew the hBN single crystals. N.W., B.Y. and W.G. wrote the paper with input from all authors.

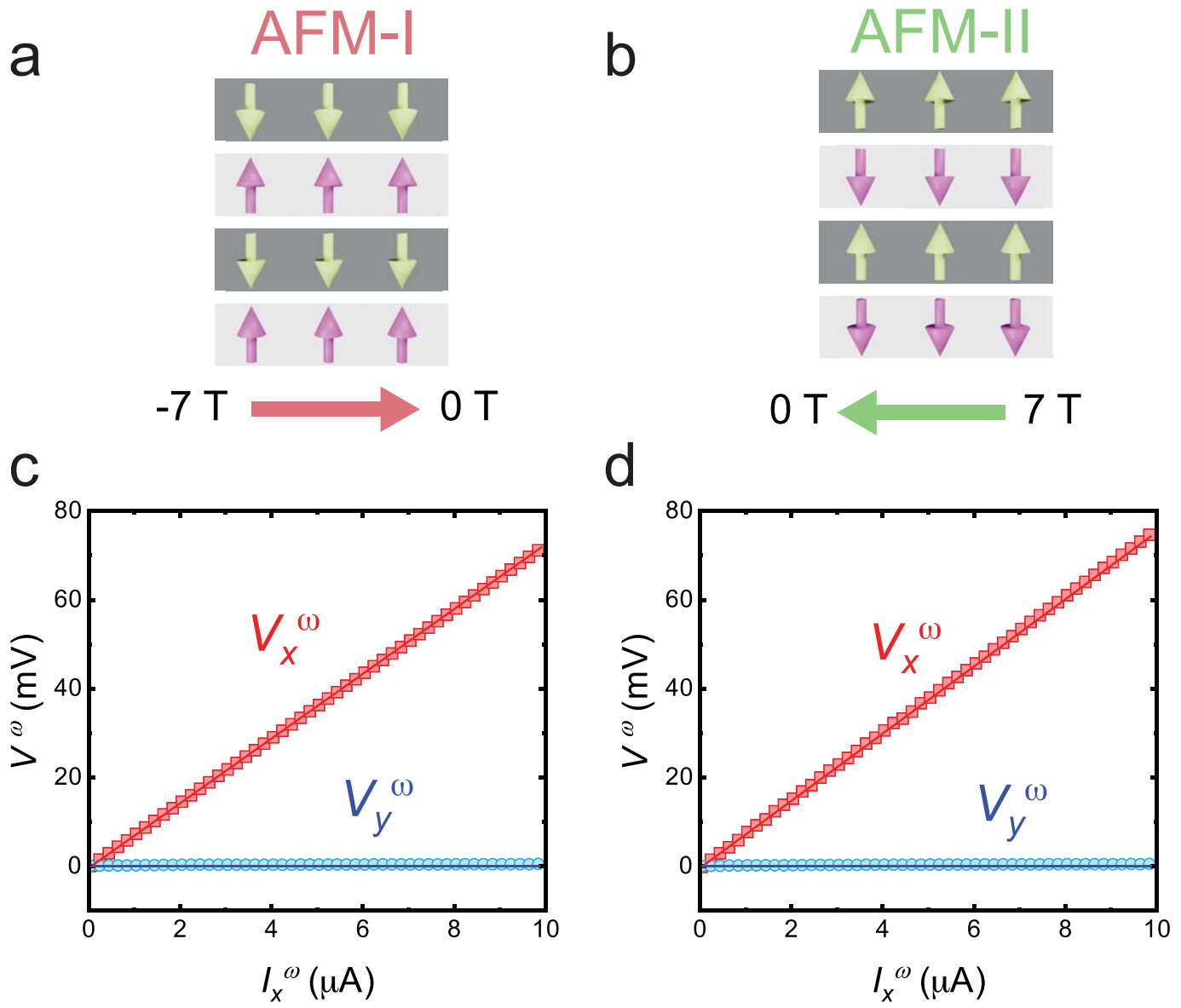
Competing interests The authors declare no competing interests.

Additional information

Supplementary information The online version contains supplementary material available at <https://doi.org/10.1038/s41586-023-06363-3>.

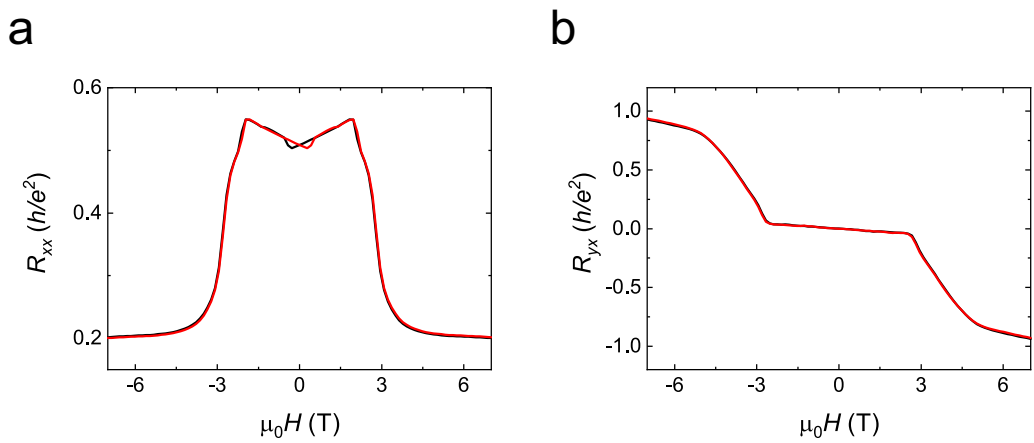
Correspondence and requests for materials should be addressed to Binghai Yan or Weibo Gao. **Peer review information** *Nature* thanks the anonymous reviewers for their contribution to the peer review of this work. Peer reviewer reports are available.

Reprints and permissions information is available at <http://www.nature.com/reprints>.



Extended Data Fig. 1 | The linear conductivity of 4SL-MnBi₂Te₄ with opposite AFM states. **a,b**, The AFM-I and AFM-II states are prepared by sweeping the magnetic field from -7 T to 0 T or +7 T to 0 T, respectively. **c,d**, The linear

longitudinal V_x^ω and transverse V_y^ω voltage as a function of current I_x^ω for AFM-I and AFM-II states, respectively. The solid line is a linear fit to the experimental data.



Extended Data Fig. 2 | The fully compensated AFM order in 4SL-MnBi₂Te₄ device. **a**, The magnetic field dependent longitudinal resistance R_{xx} of the 4SL-MnBi₂Te₄ device. **b**, The magnetic field dependent Hall resistance R_{yx} of

the 4SL-MnBi₂Te₄ device. In zero magnetic field, the AFM order is fully compensated and the Hall resistance $R_{yx} = 0$.

Extended Data Table 1 | Comparison of the nonlinear conductivity for MnBi₂Te₄ and other two-dimensional material systems

Material	T (K)	$\sigma_{xx}^{1\omega}$ (10 ⁻³ S)	$\sigma_{yxz}^{2\omega}$ (mA nm V ⁻²)	Origin
WTe ₂ (bilayer) ¹⁰	10	0.15	940	BCD
WTe ₂ (few-layer) ⁹	2	2.1	3	
Strained WSe ₂ ¹³	140	~ 0.41	~ 1200	
Twisted WSe ₂ ¹⁹	1.5	~ 0.3	~ 18000	
h-BN/graphene/h-BN ¹⁶	1.7	17.8	1.05×10^7	Skew scattering
MnBi ₂ Te ₄ (4-SL)	2	0.15	400	Quantum metric dipole
MnBi ₂ Te ₄ (6-SL)	2	0.5	2400	

The nonlinear transverse conductivity $\sigma_{yxz}^{2\omega}$ in even-layer MnBi₂Te₄ is summarized and compared with other reported material systems^{9,10,13,16,19}. The corresponding mechanisms responsible for the nonlinear response are also listed for comparison.